AGU PUBLICATIONS

JGR

Journal of Geophysical Research: Solid Earth

RESEARCH ARTICLE
10.1002/2016JB013786

Key Points:
- A new method is presented to map progress of the wetting front by neutron radiography enabling effective sorptivity to be independently calculated for two kinds low-permeability sandstone
- High-resolution X-ray computed tomography is used to characterize the microstructure of the investigated sandstone including maximum pore diameter, fractal dimension, and tortuosity
- Predictions of sorptivity are best where the pore size distribution is most uniform

Correspondence to:
Y. Zhao,
zhaoyx@cumtb.edu.cn

Citation:
Zhao, Y., S. Xue, S. Han, Z. Chen, S. Liu, D. Elsworth, L. He, J. Cai, Y. Liu, and D. Chen (2017), Effects of microstructure on water imbibition in sandstones using X-ray computed tomography and neutron radiography, *J. Geophys. Res. Solid Earth*, *122*, 4963–4981, doi:10.1002/2016JB013786.

Received 23 NOV 2016
Accepted 25 JUN 2017
Accepted article online 27 JUN 2017
Published online 18 JUL 2017

Effects of microstructure on water imbibition in sandstones using X-ray computed tomography and neutron radiography

Yixin Zhao[1,2,3], Shanbin Xue[1], Songbai Han[4], Zhongwei Chen[5], Shimin Liu[3], Derek Elsworth[3], Linfeng He[4], Jianchao Cai[6], Yuntao Liu[4], and Dongfeng Chen[4]

[1]College of Resources and Safety Engineering, China University of Mining and Technology, Beijing, China, [2]State Key Laboratory of Coal Resources and Safe Mining, China University of Mining and Technology, Beijing, China, [3]Energy and Mineral Engineering, G[3] Center and EMS Energy Institute, Pennsylvania State University, University Park, Pennsylvania, USA, [4]Neutron Scattering Laboratory, China Institute of Atomic Energy, Beijing, China, [5]School of Mechanical and Mining Engineering, University of Queensland, Brisbane, Queensland, Australia, [6]Institute of Geophysics and Geomatics, China University of Geosciences, Wuhan, China

Abstract Capillary imbibition in variably saturated porous media is important in defining displacement processes and transport in the vadose zone and in low-permeability barriers and reservoirs. Nonintrusive imaging in real time offers the potential to examine critical impacts of heterogeneity and surface properties on imbibition dynamics. Neutron radiography is applied as a powerful imaging tool to observe temporal changes in the spatial distribution of water in porous materials. We analyze water imbibition in both homogeneous and heterogeneous low-permeability sandstones. Dynamic observations of the advance of the imbibition front with time are compared with characterizations of microstructure (via high-resolution X-ray computed tomography (CT)), pore size distribution (Mercury Intrusion Porosimetry), and permeability of the contrasting samples. We use an automated method to detect the progress of wetting front with time and link this to square-root-of-time progress. These data are used to estimate the effect of microstructure on water sorptivity from a modified *Lucas-Washburn* equation. Moreover, a model is established to calculate the maximum capillary diameter by modifying the *Hagen-Poiseuille* and *Young-Laplace* equations based on fractal theory. Comparing the calculated maximum capillary diameter with the maximum pore diameter (from high-resolution CT) shows congruence between the two independent methods for the homogeneous silty sandstone but less effectively for the heterogeneous sandstone. Finally, we use these data to link observed response with the physical characteristics of the contrasting media—homogeneous versus heterogeneous—and to demonstrate the sensitivity of sorptivity expressly to tortuosity rather than porosity in low-permeability sandstones.

1. Introduction

The study of multiphase flow in porous rocks is related to a broad field with important challenges [*Bruce and Klute*, 1956; *Richards*, 1931; *Sahimi*, 2011; *Singh*, 2016; *Washburn*, 1921]. The investigation of water imbibition in porous rocks is important in a variety of contexts, including the recovery of hydrocarbons from ultralow permeability reservoirs [*Akin and Kovscek*, 1999; *Karpyn et al*., 2009; *Li and Horne*, 2001, 2013], the disposal of nuclear waste [*Hunt and Tompson*, 2005; *Sahimi*, 2011; *Tompson et al*., 2006], the sequestration of CO_2 [*Doster et al*., 2013; *Herring et al*., 2013], the environmental remediation [*Faybishenko et al*., 2005], and the protection of buildings and groundwater [*Birdsell et al*., 2015; *Cheng et al*., 2015; *Hall and Hoff*, 2012]. Several nondestructive techniques [*Roels et al*., 2004], including nuclear magnetic resonance (NMR) or magnetic resonance imaging (MRI) [*Carpenter et al*., 1993; *Leech et al*., 2003; *Pohlmeier et al*., 2008a] and γ ray attenuation [*Ferguson and Gardner*, 1963; *Nielsen*, 1972; *Nizovtsev et al*., 2008], have been applied to probe distributions of water saturation and to study the dynamics of liquid transport in porous materials. The quantitative study of water in porous media using NMR or MRI is limited by the range of pore sizes that can be imaged and the presence of paramagnetic elements in the samples [*Chen et al*., 2003; *Haber-Pohlmeier et al*., 2010; *Jelinkova et al*., 2011; *Pohlmeier et al*., 2008a]. As an alternative method to visualize fluid flow in porous materials, X-ray imaging can be applied to visualize porosity and equilibrium fluid distributions in porous materials [*Bayer*, 2005; *Nabawy and David*, 2016; *Pease et al*., 2012; *Roels and Carmeliet*, 2006; *Schillaci et al*., 2008; *Tidwell et al*., 2000]. For example, *Roels and Carmeliet* [2006] used microfocus X-ray radiography to

determine moisture content profiles at different time steps during water imbibition in ceramic brick and calcium silicate samples. *Akin et al*. [2000] studied water imbibition in diatomite (high porosity, low permeability, and siliceous rock) and Berea sandstone samples by using X-ray computed tomography (CT). They found imbibition rates of the diatomite rival and surpass those for sandstone although diatomite is roughly 100 times less permeable than sandstone. *David et al*. [2008, 2011] investigated water imbibition processes in intact and damaged porous stones using X-ray CT scanning imaging and investigate the influence of mechanical damage on fluid flow patterns. *Pons et al*. [2011] used similar methods to investigate the effect of compaction bands on water imbibition in the deformation regime formed under higher confining stresses. However, X-ray imaging is also subject to some limitations. X-rays interact with the electron cloud surrounding the nucleus of an atom, and its attenuation increases as the atomic number of the target material increases. Therefore, contrast agents (e.g., cesium chloride (CsCl) and salts) are helpful to differentiate between air and water in variably saturated porous media. However, care must be taken to ensure that the contrast agents do not alter the wetting behavior, such as contact angles and interfacial tensions [*Kim et al*., 2012].

Neutron imaging has unique advantages compared to X-ray imaging for investigating hydrogen-rich fluids in abiotic nonhydrogenous porous media [*Perfect et al*., 2014]. Neutrons interact with atomic nuclei, and this interaction does not show periodic regularity with the atomic number. Neutron imaging can easily identify light element-rich materials such as water and oil. However, it is relatively insensitive to metals such as Al [*Anderson et al*., 2009]. This unique feature of the interaction between neutron and light elements makes neutrons ideally suitable to study the fluid phase behaviors and flow of hydrogen-rich fluids within porous media. This is due to their strong attenuation by hydrogen in fluids and their relative insensitivity to both the gas phase in pores and rock constituents, such as quartz and clay minerals [*Beer and Middleton*, 2006]. However, as hydrogenous materials (e.g., water) are strongly neutron scattering and they behave as contrast agents in neutron imaging, the object under investigation should contain only trace quantities.

More importantly, recent technical improvements in neutron imaging provide adequate spatial and temporal resolution to trace water flow and to obtain quantitative information on moisture content. Researchers have observed temporal changes in the spatial distribution of water in rocks [*Dewanckele et al*., 2014; *Kang et al*., 2013], soil [*Carminati et al*., 2008; *Tullis et al*., 1994], ceramics [*Zhang et al*., 2010], sand [*Deinert et al*., 2004; *Vasin et al*., 2008], bricks [*Czachor et al*., 2002; *El Abd et al*., 2009; *Karoglou et al*., 2005], and even nanoporous glass [*Gruener et al*., 2012] using two-dimensional (2-D) neutron radiography and three-dimensional (3-D) tomography. These measurements have been conducted at various centers worldwide—at Oak Ridge National Laboratory in the USA, Paul Scherrer Institute in Switzerland, Helmholtz-Zentrum Berlin in Germany, and the Institute Laue Langevin in France [*Hall et al*., 2010; *Hassanein et al*., 2006; *Perfect et al*., 2014]. *Jasti et al*. [1987] were the first to acquire images of water movements in rock pores using neutron radiography. *El Abd et al*. [2009] determined the isothermal water diffusivity in fired clay brick using real-time neutron radiography. *Hassanein et al*. [2006] investigated the water imbibition in three types of porous rocks including Mansfield sandstone, porous Salem limestone, and Hindustan whetstone sampled from the state of Indiana in the U.S., by thermal neutron radiography. *Hall* [2013] extracted local fluid flow velocities from imaging analysis of the neutron radiographs to quantify differential water uptake in an initially air-dry sandstone core subjected to triaxial load compression. More recently, *Cheng et al*. [2015] presented the results of water imbibition in the fractures of Berea sandstones specifically in the initial stage of imbibition. *Kang et al*. [2013] obtained the unsaturated diffusivity function and sorptivity of Berea sandstone from neutron images of water imbibition.

However, the Berea sandstone investigated by *Kang et al*. [2013] and *Cheng et al*. [2015] was a high Silica (SiO_2) homogeneous pure sandstone with high porosity (0.19–0.25) and permeability (50–500 mD). Compared to high-porosity/permeability rocks, low-permeability rocks are fundamentally different due to the existence of extensive pores and throats in micron and submicron size range and the dominance of high capillary effects. Water imbibition in low-permeability sandstone with micron and even submicron pores also has broad engineering applications. For example, spontaneous imbibition is perhaps the most important phenomenon in oil recovery from fractured reservoirs [*Akin and Kovscek*, 1999] and for carbon capture and storage where capillary imbibition significantly influences the trapping of CO_2 in ultralow permeability sandstone saline aquifers [*Herring et al*., 2013; *Xie et al*., 2016].

Until now, water imbibition behavior in low-porosity/permeability sandstone has not been fully characterized, especially for the effect of microstructure on water imbibition in low-permeability sandstones. Although water imbibition in high-porosity/permeability sandstones can provide some guidance for the response of low-permeability sandstone, significant differences may result due to the presence of occluded and dead-end pores or clay minerals, for example. Compared with the pore size distribution in high-permeability sandstones, the pore size mainly ranges from micron to submicron in low-permeability sandstones, which means that, during the imbibition, water needs to overcome greater capillary pressure due to the existence of air bubbles inside smaller pores. Meanwhile, the swelling and degradation of the clay minerals in the small pores of sandstones can narrow down or even completely close some effective pores and as a result weakens the pore connectivity and increases tortuous of flow path, all of which will significantly influence and complicate the water imbibition behaviors. Thus, in the current research, a comprehensive study of the dynamics of water imbibition in two different types of low-permeability sandstones was performed using neutron radiography. The characterization of the microstructures in the two types (heterogeneous and homogeneous) of sandstones was obtained by high-resolution X-ray computed tomography and Mercury Intrusion Porosimetry (MIP). Transient two-dimensional water flow was followed by neutron imaging. Based on the analyses of the neutron radiographs, a new approach was proposed to determine the location of the wetting front, with the sorptivity measured for both specimens. A modified *Lucas-Washburn* (*L-W*) equation based on the three-dimensional fractal dimension of microstructure was proposed. The related results based on the new theoretical model were comparatively evaluated by the experimental results.

2. Theory Framework

The study of water imbibition in porous media can be traced back to the beginning of the twentieth century. *Lucas* [1918] and *Washburn* [1921] investigated water uptake in a single capillary tube together with the kinetic factors influencing water imbibition in porous media. The L-W equation was derived by applying the classical *Hagen-Poiseuille* (*H-P*) equation to laminar flow of a liquid meniscus in a capillary of radius r in which the capillary pressure p_c is determined by the *Young-Laplace* (Y-L) equation [*Hall and Hoff*, 2012]. The L-W equation is the basis of studying the water imbibition in porous media. However, the pore structure of natural porous media is complex and the pore dimensions vary significantly for different specimens. Thus, it is very important to characterize the pore structure of porous media and relate the microstructural features to theoretical models of spontaneous imbibition. Theoretical investigations related to microstructural effects on the imbibition process can be classified into three methods. The first is to modify the classical L-W equation by considering the tortuosity or different geometrical shapes of the fluid channels or pore structures [*Benavente et al*., 2002; *Cai et al*., 2014; *Hammecker et al*., 2004; *Kao and Hunt*, 1996]. The second is of using fractal models to quantify the pore structure in the process of spontaneous imbibition [*Cai et al*., 2010; *Li and Zhao*, 2011; *Yu et al*., 2014]. The last is of using the pore structures represented by periodic lattice or network to investigate water imbibition in a porous medium [*Dullien et al*., 1977; *Joekar-Niasar et al*., 2010; *Leventis et al*., 2000].

2.1. Sorptivity Model for Tortuosity and Geometrical Shape of Capillaries

Several classical theories have been established to describe the laminar flow of incompressible Newtonian liquid in capillary tubes [*Hall and Hoff*, 2012]. The classical H-P equation describes the flow rate q of an incompressible Newtonian liquid in a circular capillary as follows:

$$q = \frac{\pi}{128} \cdot \frac{\lambda^4 \Delta P}{\mu L} \tag{1}$$

where λ is the capillary diameter and L is the length of the capillary. ΔP represents the pressure drop along the capillary and μ is the viscosity of water.

The *L-Y* equation gives an expression of ΔP in a cylindrical capillary as

$$\Delta P = \frac{4\sigma \cos\theta}{\lambda} \tag{2}$$

where $\sigma = 0.0728$ N/m is the surface tension at the air-water interface and θ is the water-solid contact angle, normally taken as zero.

Thus, if the gravitational term is negligible, combining equations (1) and (2), the flow rate q in a circular capillary can be represented by

$$q = \frac{\pi}{128} \cdot \frac{\lambda^4}{\mu L} \cdot \frac{4\sigma \cos\theta}{\lambda} \tag{3}$$

Recently, *Cai et al*. [2014] derived a generalized model of wetting liquid mass imbibed in a porous medium represented by a bundle of capillary tubes. In this model, the tortuosity τ and geometric correction factor α were introduced to correct equations (1)–(3). Neglecting gravity effects, the infiltration velocity in a tortuous capillary can be calculated as

$$v_f = \frac{\alpha^3 \lambda \sigma \cos\theta}{8\mu} \cdot \frac{1}{L_f} \tag{4}$$

where L_f is the length of the tortuous capillary and α is the geometric correction factor to account for the irregular pore structures. α = 1 represents a capillary with a circular cross section, α = 1.094 a square, and α = 1.186 an equilateral triangle [*Pickard*, 1981].

Moreover, the average tortuosity can be defined by $\tau = L_f/L_e$ where L_e is the height/elevation of the wetting liquid [*Cai et al*., 2014]. The velocity v_f in the tortuous capillary can also be calculated by a straight line velocity v_s as $v_f = \tau \cdot v_s$. The relationship between v_f and v_s can be extended to the situation of an average imbibition velocity as $\overline{v}_f = \tau \cdot \overline{v}_s$. Here $\overline{v}_f$ is the average tortuous imbibition velocity and $\overline{v}_s$ is the average straight line imbibition velocity for a bundle of capillaries. Thus, $\overline{v}_s$ can be expressed as

$$\overline{v}_s = \frac{\overline{v}_f}{\tau} = \frac{dL_e}{dt} = \frac{\alpha^3 \lambda_e \sigma \cos\theta}{8\mu\tau^2} \cdot \frac{1}{L_e} \tag{5}$$

where λ_e represents the central tendency of the tube diameters within the capillary bundle and t is the imbibition time. Integrating the right side of equation (5) from L_e = 0 at t = 0 to L_e at time t yields

$$L_e = \sqrt{\frac{\alpha^3 \lambda_e \sigma \cos\theta}{4\mu\tau^2}} \cdot \sqrt{t} \tag{6}$$

The slope of a linear regression between the wetting front height and square root of invasion time was first termed the sorptivity by *Philip* [1957]. Based on equation (6), the sorptivity S is given as $\sqrt{\frac{\alpha^3 \lambda_e \sigma \cos\theta}{4\mu\tau^2}}$.

2.2. Sorptivity Model Based On the Fractal Geometry of Capillaries

Katz et al. [1985] and *Krohn et al*. [1988] reported that the pore size distribution of natural porous media (or capillaries) has the essential features of a fractal system. Based on the fractal characteristics of tortuous capillary tubes, *Cai et al*. [2010] modified equation (3) by neglecting the effect of gravity. The flow rate q is represented as

$$q = \frac{\pi}{128} \cdot \frac{\lambda^4}{\mu L_f} \cdot \frac{4\sigma \cos\theta}{\lambda} \tag{7}$$

Then, the total imbibition rate Q can be expressed as

$$Q = -\int_{\lambda_{min}}^{\lambda_{max}} q(\lambda) dN = \frac{\sigma \cos\theta}{32\mu} \cdot \frac{\lambda_{max}^3}{L_e \tau} \cdot \frac{\pi D_f}{3 - D_f} \cdot \left(1 - \beta^{3-D_f}\right) \tag{8}$$

where $dN = -D_f \lambda_{max}^{D_f} \lambda^{-(D_f+1)} d\lambda$ and $\beta = \lambda_{min}/\lambda_{max}$. λ_{max} and λ_{min} denote the maximum and minimum capillary diameter, respectively. According to *Feng et al*. [2004], β is between 10^{-2} and 10^{-4} for the porous rocks with fractal features of microstructure. D_f is the fractal dimension of the pore distribution.

If we may assume that the two-dimensional porosity of cross-sectional slices is equal to that in the three-dimensional specimen, then the average tortuous imbibition velocity can be calculated by $\overline{v}_f = Q/(A\phi)$. Here A represents the total cross-sectional area of the porous medium and φ is the porosity. As mentioned

Figure 1. Specimens investigated in the imbibition tests. C1 is a coarse-grained sandstone, and X1 is a silty sandstone.

above, $\overline{v}_f = \tau \cdot \overline{v}_s$ and the average straight line velocity of water imbibition in a set of curved capillary tubes can be calculated by

$$\overline{v}_s = \frac{dL_e}{dt} = \frac{\sigma \cos\theta}{32\mu} \cdot \frac{\lambda_{max}^3}{A\varphi L_e \tau^2} \cdot \frac{\pi D_f \left(1\text{-}\beta^{3-D_f}\right)}{3\text{-}D_f} \tag{9}$$

Integrating equation (9) results in

$$L_e = \sqrt{\frac{\sigma \cos\theta}{16\mu} \cdot \frac{\lambda_{max}^3}{A\varphi\tau^2} \cdot \frac{\pi D_f \left(1\text{-}\beta^{3-D_f}\right)}{3\text{-}D_f}} \sqrt{t} \tag{10}$$

Thus, the sorptivity S can be also defined by

$$S = \sqrt{\frac{\sigma \cos\theta}{16\mu} \cdot \frac{\lambda_{max}^3}{A\varphi\tau^2} \cdot \frac{\pi D_f \left(1\text{-}\beta^{3-D_f}\right)}{3\text{-}D_f}} \tag{11}$$

and the maximum capillary diameter can be calculated by

$$\lambda_{max} = \sqrt[3]{\frac{16\mu A\varphi\tau^2 S^2}{\sigma \cos\theta} \cdot \frac{3\text{-}D_f}{\pi D_f} \cdot \frac{1}{\left(1\text{-}\beta^{3-D_f}\right)}} \tag{12}$$

Based on this theoretical framework, a comprehensive analysis was performed to relate the microstructure (X-ray CT) to imbibed samples to the observed sorptivity (neutron radiography).

3. Material and Methods

3.1. The Specimen and Mineral Composition

Neutron radiography was used to observe temporal changes in the spatial distribution of the air-water front during imbibition for contrasting samples of silty (X1) and coarse-grained (C1) sandstones. The selected specimens were well suited for imaging water uptake with neutrons since they were devoid of organics and therefore extraneous hydrogen atoms—the full signal will be due to changes in water saturation, alone. The tested silty sandstone is a terrigenous clastic rock from Wuding County, Yunnan Province, in southern China, and the coarse-grained sandstone was collected in Xinjiang County, Shanxi Province, in north China. Figure 1 shows the two tested specimens. The coarse-grained sandstone shows a rough surface with visible defects. But the silty sandstone appears homogeneous with no obvious flaws. Moreover, X-ray diffraction

Table 1. Dimensions and Mineral Compositions of the Silty Sandstone X1 and the Coarse-Grained Sandstone C1 Used in the Experiment

	Diameter	Length	Mineral Species and Content (%)			Content of Clay Minerals (%)			
Sample	mm		Quartz	Potassium Feldspar	Clay Minerals (%)	Vermiculite	Illite	Kaolinite	Chlorite
X1	25.12	50.03	60.3	30.2	9.5	/	100	/	/
C1	25.02	50.14	94.5	/	5.5	55	5	35	5

(XRD) was employed to measure the mineral compositions of the rock samples. Table 1 shows the geometry of the specimens and the results of XRD analysis. Clay minerals account for ~5.5% in the coarse-grained sandstone and ~9.5% for the silty sandstone. Figure 2 shows the pore size distribution of the tested specimens based on Mercury Intrusion Porosimetry (MIP). The porosity of the silty sandstone is 15.2%, and the majority of pores are concentrated in the range of 1–5 μm. However, the porosity of the coarse-grained sandstone is 7.9%, which is almost half of that of the silty sandstone. The results of MIP also verify that the pore size distribution is bimodal. Moreover, before the imbibition tests, the permeability of the same tested specimens was measured using chemically equilibrated water. Table 2 shows the boundary conditions and the results of the permeability tests for both sandstones. It can be found that the measured liquid permeability of C1 is ~5.5 times greater than that of X1.

To ensure the quality of the imbibition experiment, the ends of both cores were trimmed and polished with the relative roughness of the end surfaces less than 0.05 mm (Figure 1). The sides of the cylindrical sample were covered with metal foil to prevent water wetting and to avoid evaporation. Prior to the imbibition experiments, the core specimens were dried for 24 h in an oven at constant temperature of 105°C until the weight was constant. The drying process may induce some damage to the clays in the pores of tested sandstones, but it will not influence the sorptivity of sandstones as reported by *Hall and Hoff* [2012].

3.2. High-Resolution X-ray CT Imaging

High-resolution X-ray CT (HRXCT) was used to better understand the microstructures of the tested sandstones. A nanoVoxel-3502E HRXCT with a maximum resolution of 0.5 μm (SanYing Precision Instruments Co, Ltd., China) was used. Figures 3a and 3c show the setup of the CT scanning system for the specimens of silty sandstone and coarse-grained sandstone. Considering the different features of the micropore structure in two tested sandstones, a cylindrical silty sandstone specimen with a diameter of 1.5 mm and a cylindrical coarse-grained sandstone specimen with a diameter of 4.6 mm were prepared for HRXCT scanning. The 4X lens CCD detector (16 bits CCD with a pixels matrix of 2048 × 2048) was selected to acquire higher resolution for the smaller silty core. The scanning voltage was 90 kV, and the current was ~20 μA. The cylindrical coarse-grained sandstone specimen with diameter of 4.6 mm was set on a metal bar and scanned at an average tube voltage of 110 kV and a target current around 22 μA using a 16 bit flat panel detector with a pixel matrix of 1152 × 1152. Figures 3b and 3d show the typical reconstructed slices of the silty sandstone with the resolution of 1 μm and the coarse-grained sandstone with the resolution of 3.92 μm.

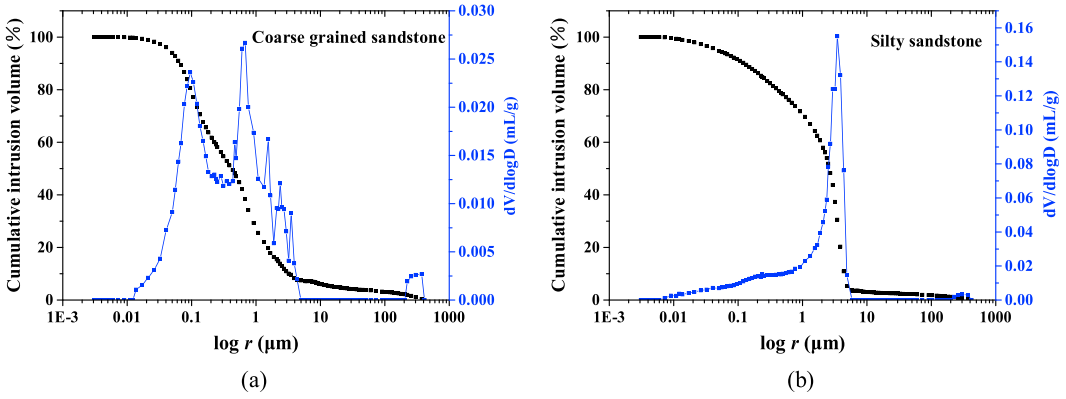

Figure 2. Cumulative mercury intrusion and pore size distribution curves based on the results of MIP experiments. Here d*V*/d(log*D*) is the log differential intrusion versus diameter. (a) Coarse-grained sandstone. (b) Silty sandstone.

Table 2. Measured Permeabilities of the Silty Sandstone X1 and the Coarse-Grained Sandstone C1

Sample	Confining Pressure (MPa)	Measure of Area (cm^2)	Viscosity (cp)	Flowrate (mL/min)	Osmotic Pressure (MPa)	Permeability (mD)	Temperature (°C)	Reynolds Number
X1	3	4.727	0.859	0.50	1.906	0.401	28.2	1.026
C1	3	4.906	0.864	0.50	0.339	2.21	27.9	0.983

The microstructures of the specimens were reconstructed and analyzed by using 3-D image analysis software Avizo (FEI Co., USA). A volume of interest (VOI) of 630 × 630 × 630 voxels in the coarse-grained sandstone and a VOI of 700 × 700 × 700 voxels in the silty sandstone were selected for further calculation of the 3-D fractal dimension and the tortuosity of the pore structures. Here the 3-D volumetric porosities of microstructures were determined using the Avizo quantification module. The tortuosity of pores was calculated using the Avizo *Centroid Path Tortuosity* module (Thermo Fisher Scientific & FEI, Avizo User's Guide, 2013, https://www.fei.com/software/avizo-3d-user-guide.pdf). To select optimal thresholds for the segmentation of pores in the two types of sandstone, the effects of thresholds on the 3-D volumetric porosities and tortuosity of pores were calculated and listed in Table 3. The Otsu method [*Otsu*, 1979; *Boone et al.*, 2014; *Korvin*, 2016; *Sekkat et al.*, 2011; *Zhang et al.*, 2015]—an auto threshold selection method exploited in Avizo *Auto Thresholding* module—was used to obtain the relationships between threshold and calculated porosity for two types of sandstone. By comparing the calculated porosity with the measured porosity by MIP, 54 and

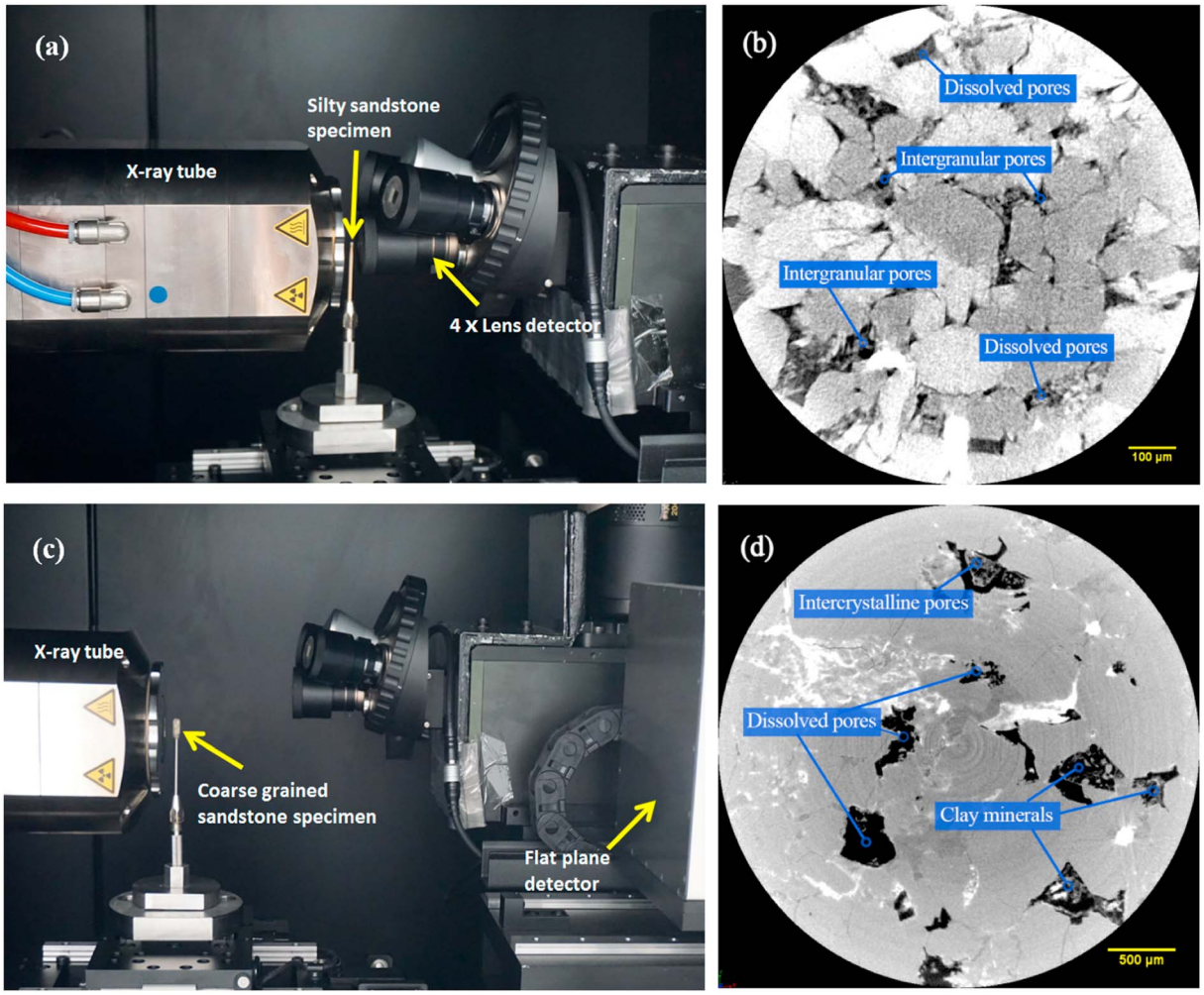

Figure 3. The setup of the scanning system and typical CT slices for the silty sandstone and the coarse-grained sandstone. (a) Setup of the scanning system for the silty sandstone specimen with a diameter of 1.5 mm. (b) Typical CT slice of scanned silty sandstone and the distribution of micropores. (c) Setup of the scanning system for the coarse-grained sandstone specimen with a diameter of 4.5 mm. (d) Typical slice of scanned coarse-grained sandstone and related micropore profiles.

Table 3. The Evolution of Porosity and Tortuosity of Two Types of Sandstones Based On the CT Images With Different Thresholds

Threshold	Porosity	Tortuosity
	Silty Sandstone	
21	0.0052	10.0817
22	0.00678	8.85729
23	0.00873	7.80619
24	0.01111	7.10245
25	0.01394	6.32792
26	0.01722	6.05599
27	0.02094	5.6314
28	0.02506	5.22295
29	0.02954	4.89063
30	0.0343	4.64157
31	0.03927	4.42031
32	0.04434	4.16155
33	0.04948	3.9376
34	0.05463	3.81615
35	0.05971	3.65618
36	0.06472	3.4965
37	0.06963	3.38214
38	0.07444	3.27206
39	0.07912	3.18799
40	0.0837	3.09265
41	0.08819	3.00924
42	0.09262	2.93601
43	0.09699	2.89139
44	0.101338	2.85097
45	0.105677	2.79409
46	0.110034	2.7328
47	0.114434	2.69331
48	0.118942	2.65682
49	0.12353	2.61235
50	0.128289	2.56785
51	0.133277	2.52465
52	0.138585	2.47642
53	0.144339	2.43594
54	0.150738	2.37442
	Coarse-Grained Sandstone	
13	0.0127	10.2677
14	0.01944	7.21301
15	0.02609	5.53862
16	0.03178	4.60887
17	0.0366	4.25879
18	0.04087	4.02893
19	0.04478	3.84584
20	0.04838	3.69279
21	0.05174	3.58723
22	0.05489	3.49301
23	0.05785	3.42438
24	0.06067	3.36552
25	0.06348	3.31258
26	0.06666	3.2578
27	0.07164	3.18666
28	0.08502	2.89456
29	0.10774	2.60778
30	0.15628	2.15749

27 were set as the thresholds to segment the pore volume in the VOIs of the silty sandstone and the coarse-grained sandstone, respectively. Then the segmented pore volumes were further processed by the Avizo *Separate Objects* algorithm to generate a *Label Field* using a watershed-based separation algorithm. This segmentation assigns a label to each pixel to describe different pores with the pixel. The segmentation is the prerequisite for accurate quantification such as volume measurement of the pore. Results of the segmentation were stored in a separate data object called a Label Field. The maximum pore diameter was measured by quantitative analysis of the separated Label Field using the Avizo *Label Analysis* module (Avizo User's Guide, online report, 2013). Figures 4 and 5 show the 2-D and 3-D representations of the microstructures in the silty sandstone and the coarse-grained sandstone after segmentation and separation with the selected threshold.

3.3. Experimental Setup for Neutron Radiography

The neutron radiography was performed at the cold neutron guide B located in the guide hall of the China Advanced Research Reactor in the China Institute of Atomic Energy. Figures 6a and 6b illustrate the experimental setup and schematic of the neutron imaging facility. To improve image quality, the experimental setup is located next to the end of the beam guide, resulting in a L/D (the ratio of the collimator tube length to its aperture diameter) of 85. There is no additional circular pinhole neutron aperture at the end of the guide. The neutron flux rate was $1.03 \times 10^7 n/cm^2/s$ when the reactor operated at 20 MW power. The facility provides most neutrons between wavelengths of 0.8 and 10 Å (with a peak at 2.9 Å). The detector was equipped with a 100 μm thick Li^6F/ZnS (Ag) scintillator and a DW936 Ikon_L ANDOR CCD camera system, giving a spatial imaging resolution of 130 μm [*Han et al.*, 2013]. This resolution is a total resolution that contains the optical resolution of CCD camera and scintillator, measured by a modulation transfer function method [*Lewandowski et al.*, 2012]. The exposure time for specimens X1 and C1 are 12 s and 2 s, respectively. In

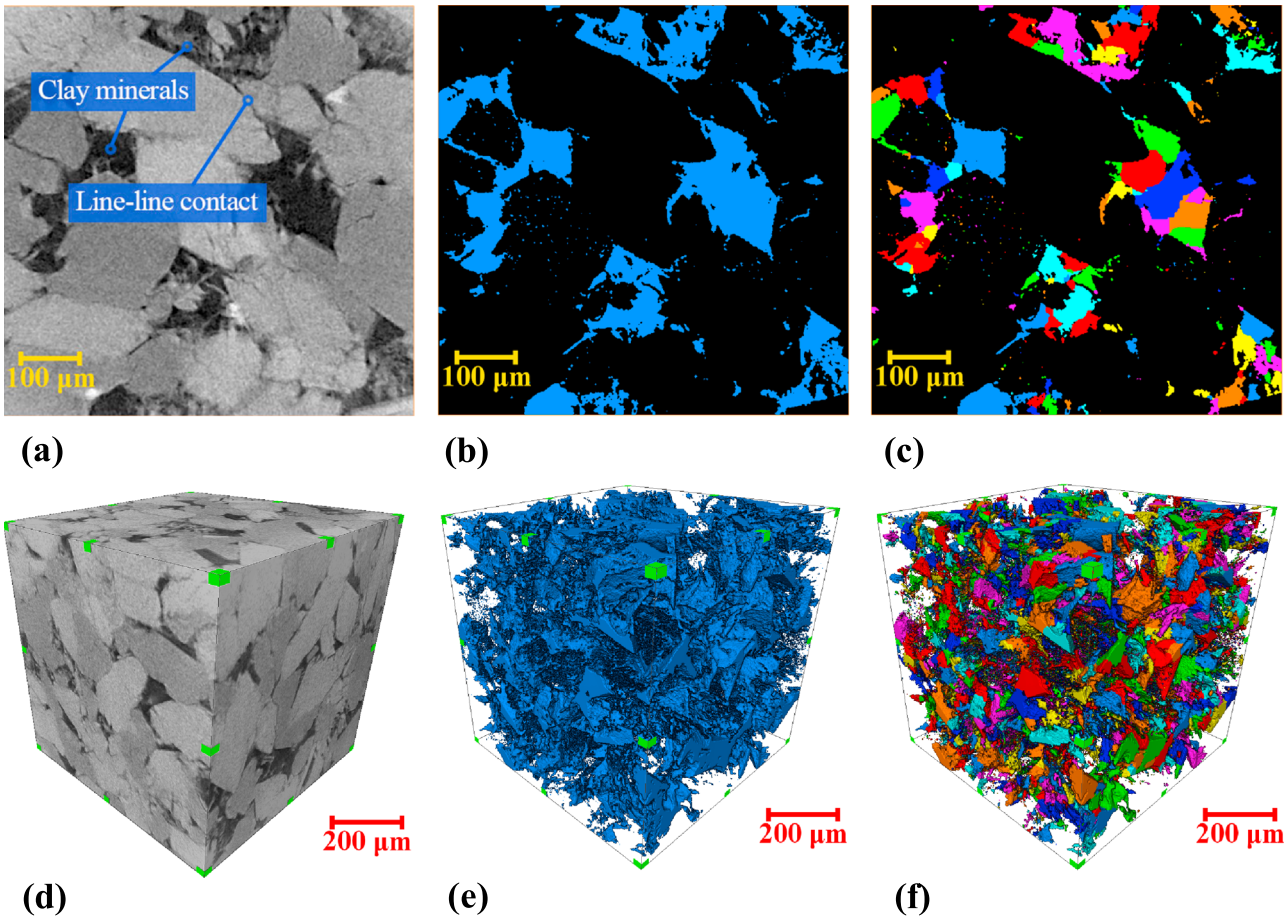

Figure 4. Segmentation and reconstruction of the silty sandstone. (a) The region of interest in the CT slice of the silty sandstone. (b) The 2-D representations of the microstructures in the silty sandstone after segmentation with a threshold of 54. (c) The generated Label Field to explore the 2-D structure of micropores based on the results of watershed-based separation algorithm. Label fields in Avizo are used to store and represent the results of an image segmentation process. Here different pores are labeled separately. (d–f) The 3-D representations of microstructures corresponding to Figures 4a–4c, respectively. The individual pores are colored differently at random in Figures 4c and 4f.

order to reduce dark current noise, the CCD camera was equipped with a Peltier cooling system and routinely cooled down to −60°C. For these measurements, the field of view is approximately 10 cm × 10 cm.

The experimental protocol includes the following: (1) obtain 10 flat field images (shutter opened without specimen) and then 10 dark current images (shutter closed, no neutron illumination), respectively; (2) place the specimen on the scintillator screen as shown in Figure 6c and take 10 images of the dried specimen; and (3) measure and monitor the water front invasion on a continuous time basis. An aluminum container is used to supply water and placed on an elevatable platform. The aluminum container is filled with distilled water to a depth of 1 cm. During the monitoring of the water front, the water container is gradually raised until the base of the specimen (approximately 5 mm) contacts the free surface of the water—this moment is defined as zero time. Images acquired from this moment are denoted as $I_{(\mathrm{Wet})}$. Because of the limitation of the experiment time for specimen X1, a total of 161 raw images was obtained and 54 images were processed to calculate the sorptivity in a time interval of ~41 s. This also causes the final water front to remain lower than 25 mm in the specimen (X1). For specimen C1, a total of 55 images was selected from 4545 raw images to calculate the sorptivity. The time interval is 40 s for the first 20 selected images and 200 s for the remaining 35 images.

3.4. Neutron Image Processing and Parameter Estimation

For a monochromatic (single wavelength) beam traversing a homogeneous specimen, the measured intensity T is given by the *Lambert-Beer* law [*Anderson et al.*, 2009]

$$T/T_0 = \mathrm{e}^{-\gamma\omega_{(t)}} \tag{13}$$

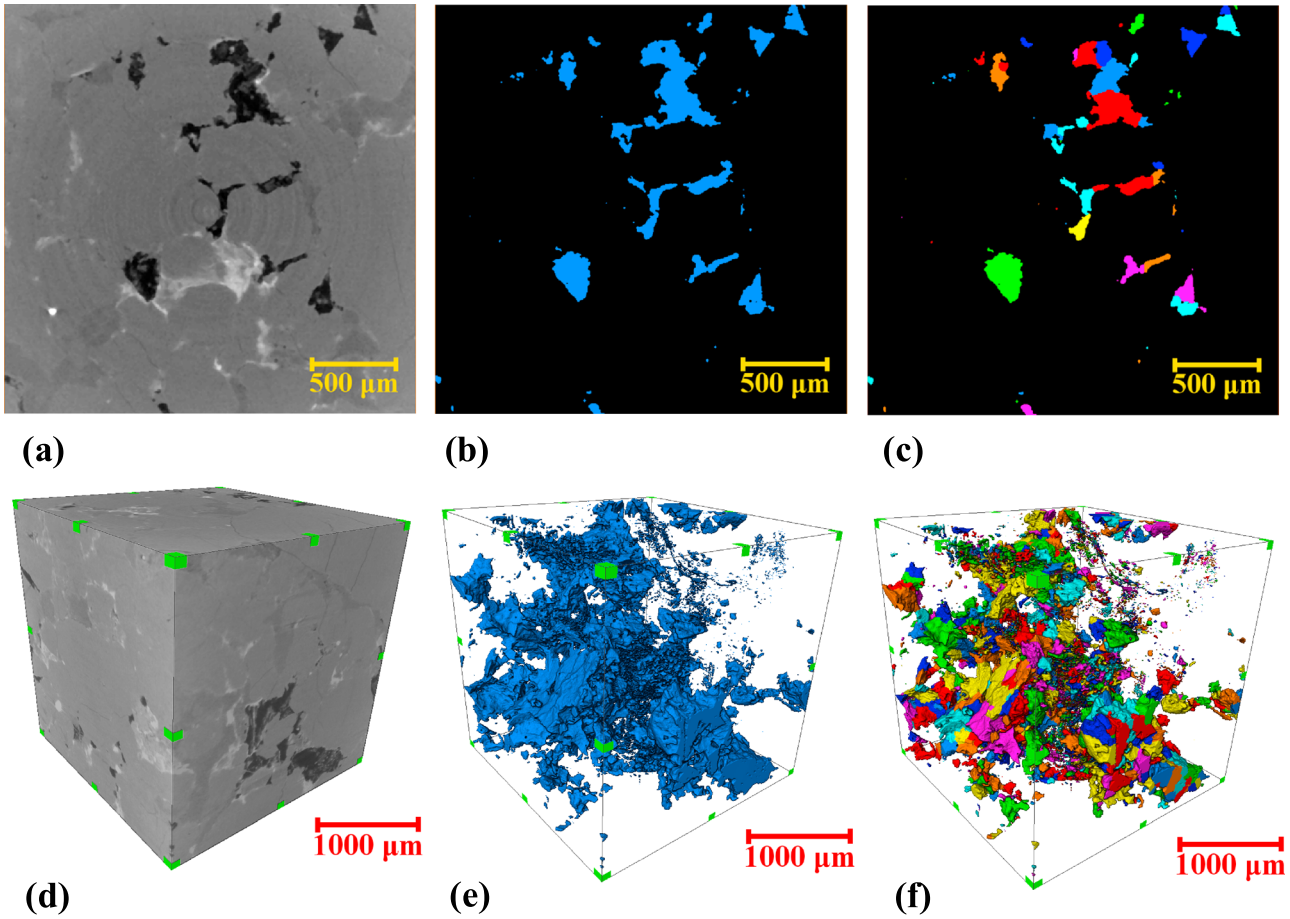

Figure 5. Segmentation and reconstruction of the coarse-grained sandstone. (a) Region of interest in the CT slice of the coarse-grained sandstone. (b) The 2-D representations of the microstructures in the coarse-grained sandstone after segmentation with a threshold of 27. (c) Generated Label Field to explore the structure of micropores based on the results of watershed-based separation algorithm. (d–f) The 3-D representations of microstructures corresponding to Figures 5a–5c, respectively. The individual pores are colored differently at random in Figures 5c and 5f.

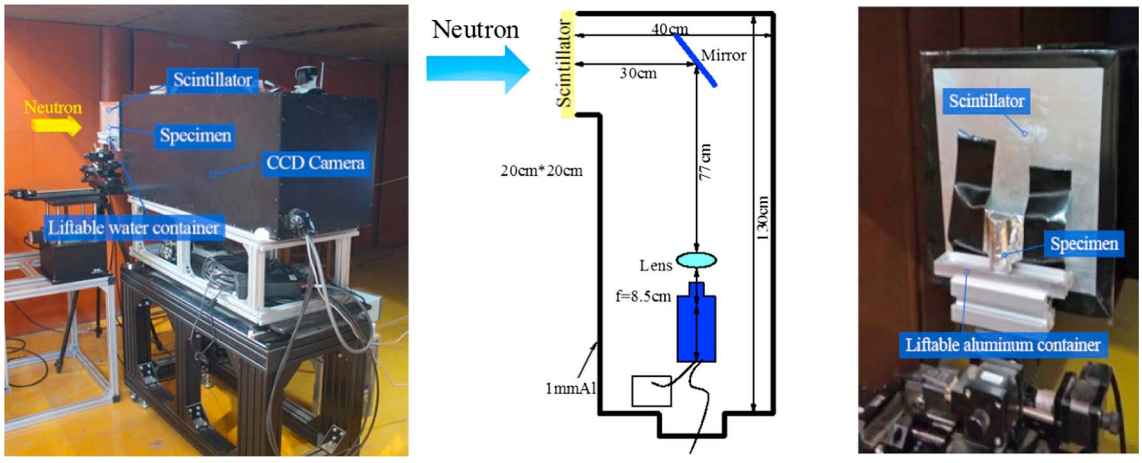

Figure 6. Experimental arrangement for monitoring water imbibition by neutron radiography. (a) Experimental setup. (b) Schematic of neutron imaging facility at the China Advanced Research Reactor. (c) Details of the specimen position.

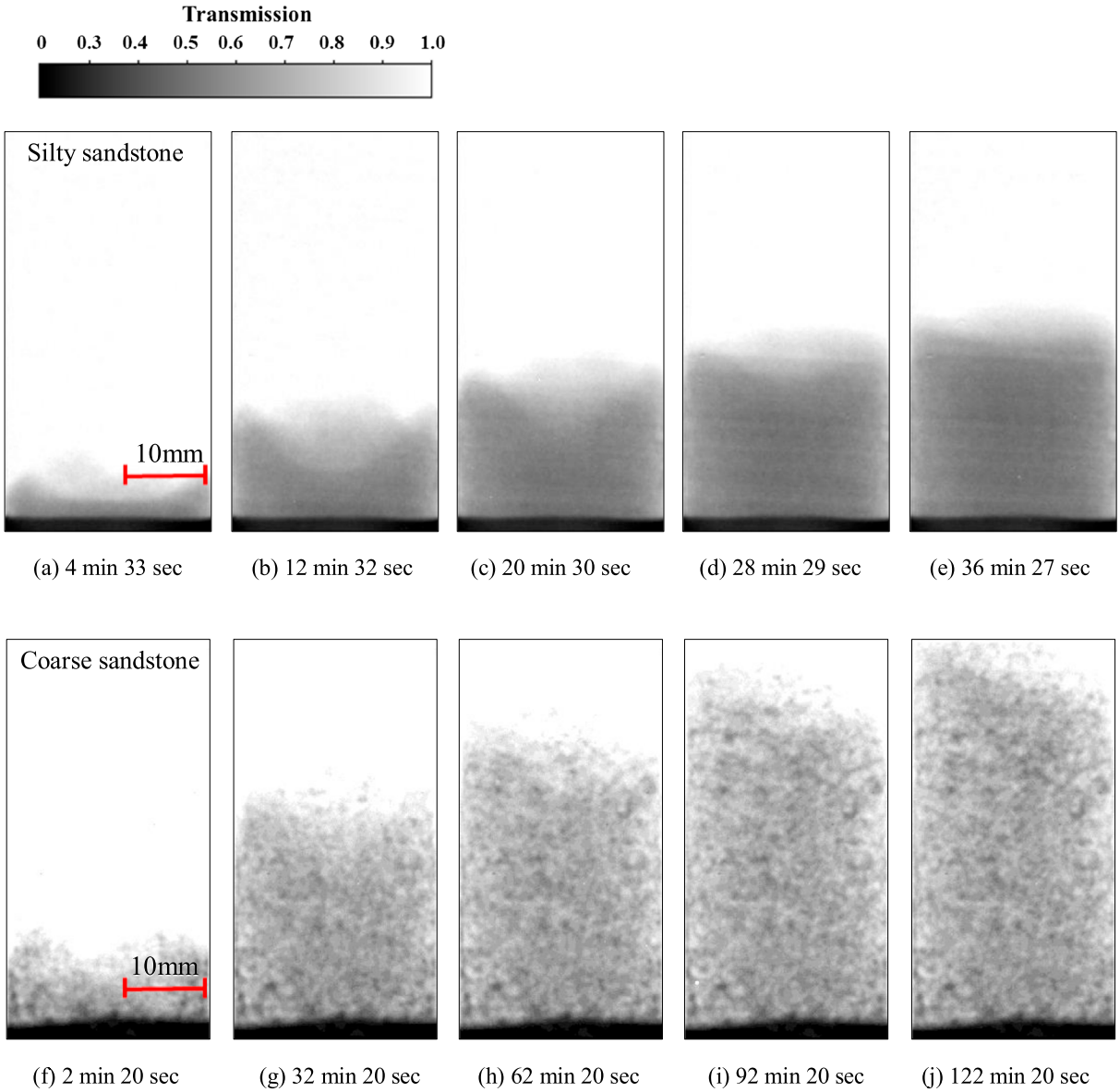

Figure 7. Selected net water transmission images of water imbibition in the tested specimens. (a–e) Typical sequential images of water imbibition in silty sandstone (X1) at various time. (f–j) Typical neutron radiographies of water imbibition in coarse-grained sandstone C1 at various times. In these images, the effects of dry specimens, aluminum foil, and background have been removed—only the signal for water remains. Darker area denotes higher moisture content.

where T is the transmitted intensity, T_0 is the original intensity, γ is the attenuation coefficient of water, and $\omega_{(t)}$ is the time-dependent water thickness along the direction of neutron beam.

All images were processed and analyzed by the *ImageJ* software packages [*Abramoff et al*., 2004; *Rasband*, 1997–2016; *Schneider et al*., 2012]. For each acquired image, the two-dimensional distribution of water within both tested specimens was determined as follows. First, the median intensities of 10 flat field images and 10 dark current images were picked to reconstruct one Open Beam reference image $I_{(OB)}$ and one Dark Field reference image $I_{(DF)}$. The dry reference image $I_{(Dry)}$ was obtained which is the median of the 10 images of the dry specimen. The median value of the 10 images was chosen for each pixel since it is less likely that all 10 images have detected gamma ray contamination for the same pixel [*Kim et al*., 2013]. Then $I_{(Wet)}$ and $I_{(Dry)}$ were normalized with respect to $I_{(OB)}$ and $I_{(DF)}$ as described by equation (14) to remove detector background noise, fluctuations in the neutron flux, and the heterogeneities in the beam and detector [*Kang et al*., 2014]. Then the area of interest was cropped.

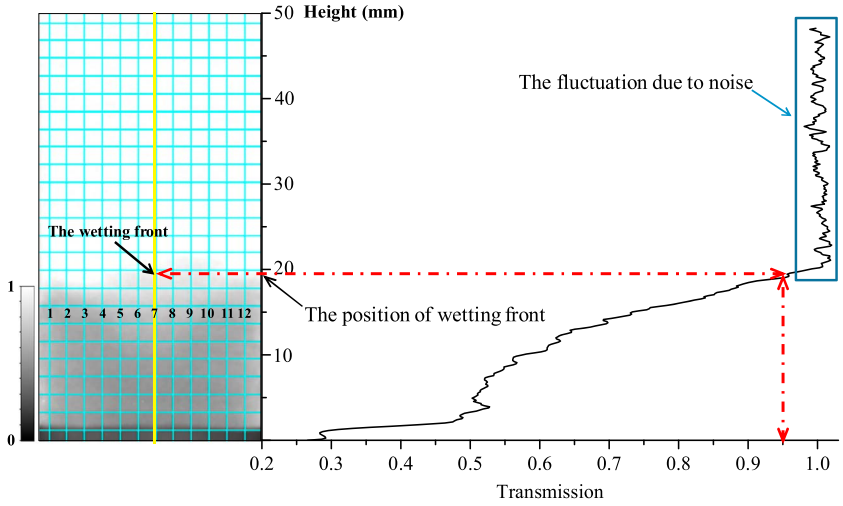

Figure 8. Schematic of the method for identifying the wetting front in the specimens. (left) Location of the 12 vertical net water transmission profiles in the specimen and typical transmission image of net water imbibition in X1 at 18 min 27 s. (right) The distribution of the transmission along the #7 monitoring line (the vertical yellow line in the left) in specimen X1 at 18 min 27 s.

$$I'_{(\mathrm{Wet})} = f_k \cdot \frac{I_{(\mathrm{Wet})} - I_{(\mathrm{DF})}}{I_{(\mathrm{OB})} - I_{(\mathrm{DF})}} \tag{14}$$

In equation (14), $I_{(\mathrm{Wet})}$ can be substituted by $I_{(\mathrm{Dry})}$ to obtain $I'_{(\mathrm{Dry})}$. For the same specimen, all the images were acquired under the same power of the neutron beam, the rescaling factor f_k used to correct the fluctuations in the neutron flux was taken as unity in this work.

The normalized wet images $I'_{(\mathrm{Wet})}$were divided by the normalized dry images $I'_{(\mathrm{Dry})}$ to obtain the net water transmission images I_n. Any attenuation effects associated with minerals in the specimen and the aluminum foil tape were removed from images I_n. The transmission of images I_n on a pixel-by-pixel basis was set equal to T/T_0. The selected net water transmission images of specimens X1 and C1 are shown in Figure 7. Based on equation (13), it can be concluded that the smaller the transmission of the images I_n, the larger the water content.

One net water transmission image of X1 is shown in Figure 8a. The area of interest in X1 is 25×48.36 mm^2. The 4 mm^2 cyan grids were superimposed on the image to define 12 vertical lines for monitoring the change of transmission with time. The same approach was applied to specimen C1. The net water transmission profiles along the vertical direction of the specimen were extracted from the images. For instance, the yellow line in Figure 8a shows the #7 monitoring line of the wetting front in specimen X1 at a time of 18 min 27 s. The distribution of the transmission along the #7 monitoring line is shown in Figure 8b. The transmission increases in the direction of the water imbibition. Figure 8b shows the wetting front (i.e., its position) where the value of the transmission is equal to or exceeds a threshold value indicating a wetting phase. The dry and wet samples have different transmission values because the water can absorb the neutron signal. To reduce the effects of the transmission fluctuation due to the noise of image, the various threshold values were tried for both tested sandstones to analyze the wetting front position. Finally, the threshold value for sample X1 is 0.95 and 1.00 for sample C1 based on the average transmission value of the dry image for each sample. During our tests, if the longitudinal transmission exceeds the threshold values, the specimens were assumed unwetted by water. The lateral boundary of the wetting line represents the water imbibition interface in the specimen.

4. Results and Discussion

4.1. Water Wetting Front Determination and Its Evolution

The Bond number (B_o) is a dimensionless value that can be used to demonstrate the gravity that can be neglected under the conditions of our tests [*Cheng et al.*, 2015]. The equation for Bond number is

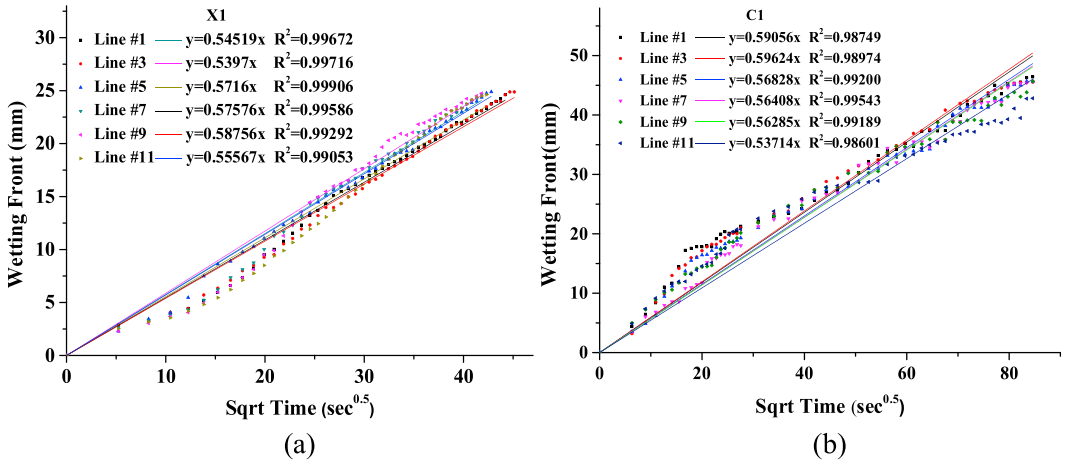

Figure 9. The relationships between the wetting front of six typical monitored profiles and the square root of imbibition time in both tested specimens. The selected vertical monitored profiles are #1, #3, #5, #7, #9, and #11. The straight lines show the linear fitting results for specimens X1 and C1. The slope of the linear regression defines the sorptivity. (a) Silty sandstone sample X1. (b) Coarse grain sandstone sample C1.

$B_O = \rho \cdot g \cdot k_w/\sigma$. Here the density of water is $\rho = 1000$ kg m^{-3}, the air-water interfacial tension is $\sigma = 0.0728$ N/m at 20°C, and the gravitational acceleration is $g = 9.81$ m s^{-2}. k_w represented intrinsic permeability of the rock which can be found in Table 2. Thus, the Bond number is 5.33×10^{-11} for the silty sandstone and 2.94×10^{-10} for the coarse grain sandstone, which are much smaller than one. So the contribution of gravity can be ignored in our experiment. At macroscopic scale, spontaneous imbibition associated with a uniform wetting front occurs in a homogenous porous medium when water displaces dry air. This macroimbibition phenomenon can be simplified as a one-dimensional problem. Considering the complexity of microstructures in the tested sandstones, 12 vertical net water transmission profiles were set for each specimen, as shown in Figure 8a. The net water wetting front was monitored in space (laterally) and in time.

The relationships between the wetting front of six typical monitored profiles and the square root of imbibition time were plotted in Figure 9. It clearly shows that water uptake correlates with the square root of time for both rock specimens. The 12 sorptivities along the monitored profiles were estimated by using linear regression, and the average values of goodness of fit (R^2) for both X1 and C1 were larger than 0.99, as listed in Table 4.

Table 4. Sorptivity (S) and Goodness of Fit (R^2) Parameters of the Silty Sandstone X1 and the Coarse-Grained Sandstone C1[a]

Monitoring Lines	X1		C1	
	Parameters			
	S (mm s$^{-0.5}$)	R^2	S (mm s$^{-0.5}$)	R^2
Line 1	0.54519	0.99672	0.59056	0.98749
Line 2	0.54924	0.99784	0.60493	0.98599
Line 3	0.53970	0.99716	0.59624	0.98974
Line 4	0.55256	0.99923	0.58112	0.98809
Line 5	0.57160	0.99906	0.56828	0.99200
Line 6	0.57749	0.99787	0.57130	0.99238
Line 7	0.57576	0.99586	0.56408	0.99543
Line 8	0.58079	0.99449	0.57127	0.99335
Line 9	0.58756	0.99292	0.56285	0.99189
Line 10	0.57309	0.99224	0.53056	0.99044
Line 11	0.55567	0.99053	0.53714	0.98601
Line 12	0.56516	0.99602	0.52205	0.98455
Average value	0.56430	0.99596	0.56730	0.99068

[a]The average values were calculated by ignoring the maximum and minimum values.

In addition, the wetting front as a function of lateral position and square root of time are shown in Figure 10. Ignoring the maximum and minimum values, the average sorptivity is 0.5643 mm s$^{-1/2}$ for X1 and 0.5673 mm s$^{-1/2}$ for C1. These sorptivity results are much smaller than those reported for Berea sandstone matrix sorptivities ranging from 2.90 to 4.55 mm s$^{-1/2}$, which were captured within very early time of imbibition [*Cheng et al.*, 2015]. This means that the conclusion proposed by *Cheng et al.* [2015] that sorptivities increased linearly with the increase of the permeability does not apply in the current investigation. Moreover, it was found that the sorptivities are almost the same, although there is a dramatic difference in porosity and pore size distribution

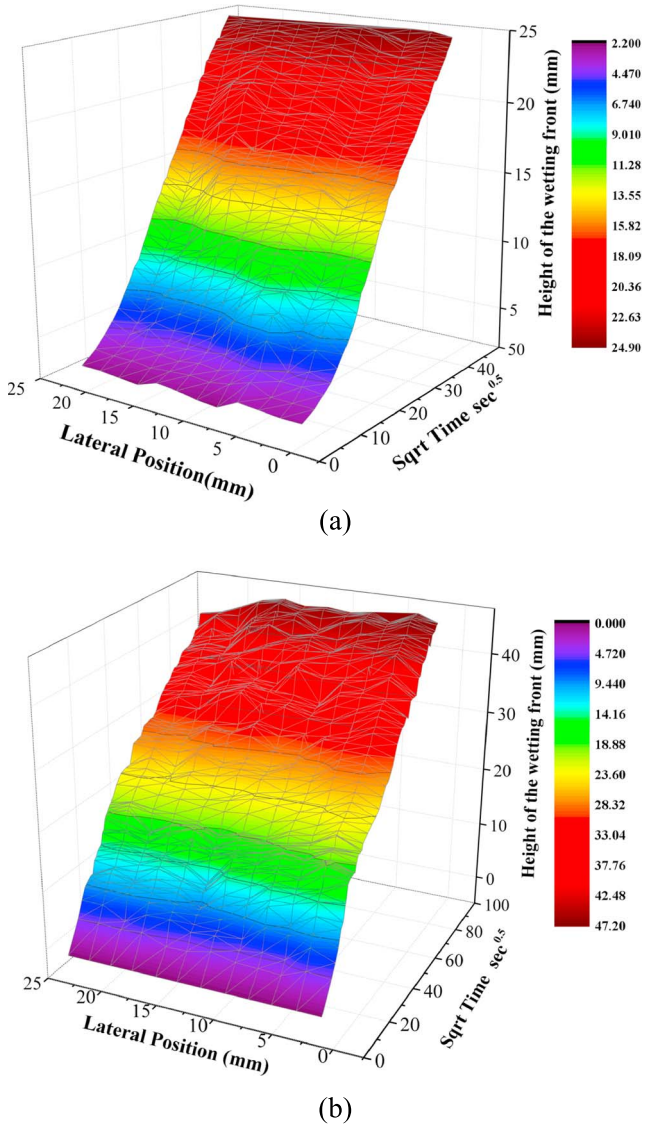

Figure 10. Relationship between the wetting front height, lateral position, and square root of time in two tested sandstones. Here the time unit is seconds and the colors identify the height of the water front. (a) Silty sandstone X1 and (b) coarse-grained sandstone C1.

between X1 and C1. As listed in Table 4, the results of sorptivity in the tested sandstones are consistent with those (sorptivity ranges from 0.10 to 1.72 mm $s^{-1/2}$) obtained by *Hammecker and Jeannette* [1994] for capillary-driven water uptake in sandstones. They are also consistent with the results determined by *Hassanein et al.* [2006] by means of thermal neutron radiography for spontaneous imbibition of water in porous Salem limestone (0.84 mm $s^{-1/2}$) and Hindustan whetstone (0.51 mm $s^{-1/2}$).

4.2. Effect of Microstructure in Tested Sandstones on Sorptivity

According to *Hall and Hoff* [2012], water transport behavior in porous rocks is greatly influenced by microstructure, such as porosity and pore size and their respective distributions. In this section, the effects of microstructure on sorptivity are discussed. The predicted sorptivities S_p of specimens X1 and C1 were also calculated based on equation (6). The parameters used to calculate the minimum predicted sorptivities $S_{p\text{-min}}$ and associated results are listed in Table 5. Here the average pore diameter λ_e was measured by MIP and the tortuosity τ was calculated based on the 3-D segmented pore volume as shown in Figures 4e and 5e.

4.2.1. Silty Sandstone Specimen X1

The predicted sorptivity for specimen X1 can be expressed as $S_p = 0.89078\sqrt{\alpha^3}$ based on equation (6). Because $\alpha \geq 1$, the predicted sorptivity is $S_p \geq 0.89078$. Thus, the minimum predicted sorptivity $S_{p\text{-min}}$ of the silty sandstone is 1.5 times larger than the sorptivity measured by the water imbibition test. It suggests that the average pore diameter λ_e of the silty sandstone measured by MIP is larger than the effective capillary diameter, or the assumed tortuosity is underestimated. As shown in Figure 4, there are some infilling materials (clay minerals and quartz grains) within the pores, which will not only reduce the effective seepage radius of the pores but also increase the tortuosity of flow. Moreover, illite dominates the clay minerals in the silty sandstone, with the possibility of swelling and pore blockage once contacted by water. The above features likely contribute to the measured lower sorptivity of the silty sandstone compared with that estimated from the measured pore structure. Thus, the effective porosity controlling imbibition may

Table 5. Parameters Used to Estimate the Sorptivity and the Associated Calculation Results

Sample	μ (Ns/m^2)	τ	σ (N/m)	θ	λ_e (μm)	S (mm/s$^{-0.5}$)	$S_{p\text{-min}}$ (mm/s$^{-0.5}$)
X1	0.001	2.3744	0.0728	0	0.2458	0.5643	0.89078
C1	0.001	3.1867	0.0728	0	0.1589	0.5673	0.53365

Table 6. Parameters used to Estimate the Maximum Capillary Diameter of Two Tested Sandstones and the Results of λ_{max1}, λ_{max2}, and $\lambda_{max\text{-}ct}$

Sample	D_f	φ	β	λ_{max1} (μm)	λ_{max2} (μm)	$\lambda_{max\text{-}ct}$ (μm)
X1	2.4036	0.1507	10^{-3}	132.8250	180.0778	119.0045
C1	2.1903	0.0716	10^{-3}	143.9318	138.1823	338.446

be overestimated by analyzing the CT images of dry specimen since it introduces an underestimation of the tortuosity. Finally, the spatial microstructure will contribute to a low capillary diameter and a high tortuosity for water imbibition in the silty sandstone.

4.2.2. Coarse-Grained Sandstone Specimen C1

The predicted sorptivity for specimen C1 is evaluated as $0.53365\sqrt{\alpha^3}$, resulting in a predicted sorptivity of $S_p \geq 0.53365$ as $\alpha \geq 1$. Thus, the sorptivity measured by the previous water imbibition test is 1.06 times larger than the minimum predicted value $S_{p\text{-}min}$. Compared to the predicted sorptivity of the silty sandstone, equation (6) gives a closer estimate for the coarse-grained sandstone.

Table 5 shows that the minimum predicted sorptivity $S_{p\text{-}min}$ and the measured sorptivity S are ~40% and ~0.53% larger than that of the silty sandstone. But the porosity of the coarse-grained sandstone is 7.16%, which is nearly half of that of the silty sandstone. Previous research has noted that rocks with the porosity lower than ~10% may have poor pore connectivity due to the shrinkage, closure, and elimination of the pore throats [*Benavente et al*., 2015; *Doyen*, 1988; *Wong et al*., 1984]. Figure 5e also verifies the poor connectivity of the coarse-grained sandstone. A low connectivity also likely results in a high tortuosity and low sorptivity of the coarse-grained sandstone. Thus, the pore size, clay minerals, and porosity control the capillary diameter and tortuosity and further determine the sorptivity during water imbibition in the low-permeability regime.

4.3. Determination of the Maximum Capillary Diameter for Sorptivity

Previous results indicate that pore size plays a crucial role in the sorptivity of the tested sandstones. The maximum capillary diameters of the specimens (X1 and C1) may be calculated [*Cai and Yu*, 2010]. Based on equation (12) and the parameters in Tables 5 and 6, the maximum capillary diameter can be obtained. Here the maximum capillary diameters λ_{max1} and λ_{max2} are calculated based on the measured sorptivity S and the predicted sorptivity $S_{p\text{-}min}$, respectively. Because of the poor connectivity of pores in both samples, we can assume that the ratio between λ_{max} and λ_{min} is 1000. Thus, β is equal to 0.001 for both tested sandstones in our case, which is in accordance with the range of β from 10^{-2} to 10^{-4} suggested by *Feng et al*. [2004]. Table 6 shows that the values of λ_{max1} for specimens X1 and C1 are very close as ~133 μm and ~144 μm —thus, the maximum capillary diameters calculated based on the measured sorptivity S for both tested sandstones are similar. However, the λ_{max2} values calculated based on the predicted sorptivity $S_{p\text{-}min}$ for the specimens (X1 and C1) are ~180 μm and ~138 μm—thus, the maximum capillary diameter λ_{max2} in the silty sandstone is ~30% larger than that of the coarse-grained sandstone.

The maximum pore diameter for both sandstones can also be measured by analyzing the separated Label Field from 3-D CT images using the Avizo Label Analysis module (Avizo User's Guide, online report, 2013). The maximum label volumes for the silty sandstone and the coarse-grained sandstone are 8.82×10^5 μm^3 and 2.03×10^7 μm^3, respectively. Thus, the maximum equivalent diameter $\lambda_{max\text{-}ct}$ can be obtained by computing the diameter of spherical pore with the maximum label volume. It was found that the maximum equivalent diameters $\lambda_{max\text{-}ct}$ are ~119 μm (silty sandstone) and ~338 μm (coarse-grained sandstone). For the silty sandstone, the maximum equivalent pore diameter $\lambda_{max\text{-}ct}$ is close to the maximum capillary diameter λ_{max1}. However, for the coarse-grained sandstone, $\lambda_{max\text{-}ct}$ is much larger than λ_{max1}. This is mainly caused by the poor connectivity of large pores in the coarse-grained sandstone [*Benavente et al*., 2015].

To evaluate the errors caused by the assumption of pores as sphere on the value of $\lambda_{max\text{-}ct}$, the sphericities of pores in both tested sandstones are analyzed. Normally, a perfect sphere has a sphericity of one and any other shape less than one. For example, the sphericity of a cube is about 0.806 [*Wadell*, 1935]. To estimate the sphericity of pores in both tested sandstones, the data of the segmented volumes presented in Figures 4f and 5f were analyzed using the Avizo Label Analysis module. The results for sphericity for the pores in both sandstones are presented in Figure 11. The sphericity of ~70% pores in the silty sandstone and ~58% pores in the coarse-grained sandstone is in the range 0.8 to 1.0—suggesting that the assumption of the pores

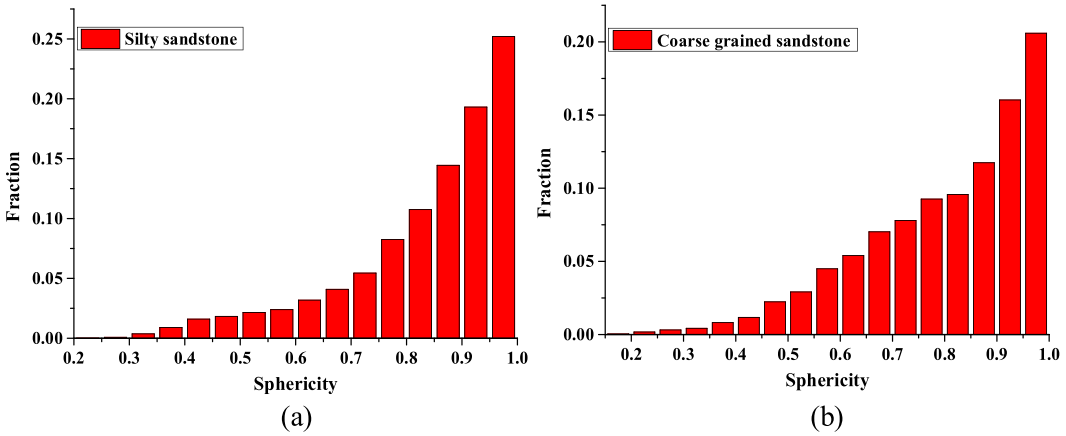

Figure 11. The results of sphericity evaluations for pores in both sandstones based on the segmented volumes presented in Figures 4f and 5f. (a) Silty sandstone. (b) Coarse-grained sandstone.

as sphere could cause relative larger error to $\lambda_{max\text{-}ct}$ of coarse-grained sandstone. Thus, λ_{max1} is believed to be the real maximum capillary diameter in the connected pores, because it is calculated based on the sorptivity S measured from the water imbibition tests.

5. Summary and Conclusions

Neutron radiography was successfully used to investigate water imbibition in two sandstone specimens with different permeabilities and heterogeneities. A new approach is proposed to acquire sorptivities of these two specimens based on the analysis of neutron radiographs. The measured results show a strong linear relationship between the measured wetting front and the square root of time—suggesting linear sorptive behavior and a constant sorptivity. The obtained results also indicate that capillary forces dominate over gravity in the early stages of water imbibition. Moreover, the calculated sorptivities are much smaller than those reported for Berea sandstone matrix. Although rock characterization using HRXCT, MIP, and XRD show significant differences between the two sandstones in terms of both mineral compositions and microstructure, the sorptivities are somewhat similar.

Through highly constrained characterization of sample microstructure, it is shown that the features of the pore microstructure, including the tortuosity, average size of connected pores, and pore shape, play a significant role in determining the sorptivity. As revealed by HRXCT, the low sorptivity can also be attributed to the presence of clay minerals within the pores. The interaction between clay minerals and water contributes to a more complex pore structure including a large tortuosity and small capillary size. Thus, it is necessary to introduce a geometric correction factor and tortuosity in the classical H-P and Y-L equations and to further modify the L-W equation to describe water imbibition in low-permeability sandstones, consistent with theory. In addition, a model was established to calculate the maximum capillary diameter by modifying the H-P and Y-L equations based on fractal theory. Comparing the calculated maximum capillary diameter with the maximum pore diameter measured by analyses of high-resolution CT images shows that media with a more homogeneous structure (silty sandstone) indeed conform most closely to theory for a monomodal pore size. We demonstrate that neutron radiography is a powerful method to capture the dynamics of spontaneous imbibition in porous and porous-fractured media since 2-D radiographs can be acquired rapidly. These results lay a foundation for the numerical simulation for the water imbibition in the tight reservoir formations.

Acknowledgments

The results presented in this article rely on the data collected at the Neutron Scattering Laboratory, China Institute of Atomic Energy. Data are available to external users upon request provided proper acknowledgement is applied in subsequent reporting. The China Institute of Atomic Energy is gratefully acknowledged for their support of this work and for providing access to the Neutron imaging facility. The authors specially thank Daoyang Jiang for his aid in the experiments and data analysis. The Editor Michael Walter and anonymous reviewers are appreciated for their comments which improved an earlier version of this paper. This research is supported by the National Key R&D Program of China (2016YFC0801401 and 2016YFC0600708), the National Natural Science Foundation of China (51174213), and the Fundamental Research Funds for the Central Universities.

References

Abramoff, M. D., P. J. Magalhaes, and S. J. Ram (2004), Image processing with ImageJ, *Biophoton. Int.*, *11*(5–6), 36–42.

Akin, S., and A. R. Kovscek (1999), Imbibition studies of low-permeability porous media, SPE 54590, Proceedings of the Western Regional Meeting, Anchorage, Alaska, 26–27 May.

Akin, S., J. M. Schembre, S. K. Bhat, and A. R. Kovscek (2000), Spontaneous imbibition characteristics of diatomite, *J. Pet. Sci. Eng.*, *25*(3–4), 149–165.

Anderson, I. S., A. J. Hurd, and R. L. McGreevy (2009), *Neutron Imaging and Applications: A Reference for the Imaging Community*, pp.199–200, Springer, New York.

Bayer, A. (2005), *X-ray Attenuation Techniques to Explore the Dynamics of Water in Porous Media*, pp. 51–60, Ruperto Carola University of Heidelberg, Heidelberg, Germany.
Beer, F. C. D., and M. F. Middleton (2006), Neutron radiography imaging, porosity and permeability in porous rocks, *S. Afr. J. Geol.*, *109*(4), 541–550.
Benavente, D., P. Lock, M. Cura, and S. Ordóñez (2002), Predicting the capillary imbibition of porous rocks from microstructure, *Transp. Porous Media*, *49*(1), 59–76.
Benavente, D., C. Pla, N. Cueto, S. Galvañ, J. Martínez-Martínez, M. A. García-del-Cura, and S. Ordóñez (2015), Predicting water permeability in sedimentary rocks from capillary imbibition and pore structure, *Eng. Geol.*, *195*, 301–311.
Birdsell, D. T., H. Rajaram, D. Dempsey, and H. S. Viswanathan (2015), Hydraulic fracturing fluid migration in the subsurface: A review and expanded modeling results, *Water Resour. Res.*, *51*, 7159–7188. doi:10.1002/2015WR017810.
Boone, M. A., T. De Kock, T. Bultreys, G. De Schutter, P. Vontobel, L. Van Hoorebeke, and V. Cnudde (2014), 3D mapping of water in oolithic limestone at atmospheric and vacuum saturation using X-ray micro-CT differential imaging, *Mater. Charact.*, *97*, 150–160.
Bruce, R. R., and A. Klute (1956), The measurement of soil moisture Diffusivity1, *Soil Sci. Soc. Am. J.*, *20*(4), 458–462.
Cai, J., and B. Yu (2010), Prediction of maximum pore size of porous media based on fractal geometry, *Fractals*, *18*(04), 417–423.
Cai, J., B. Yu, M. Zou, and L. Luo (2010), Fractal characterization of spontaneous co-current imbibition in porous media, *Energy Fuels*, *24*(3), 1860–1867.
Cai, J., E. Perfect, C. L. Cheng, and X. Hu (2014), Generalized modeling of spontaneous imbibition based on Hagen-Poiseuille flow in tortuous capillaries with variably shaped apertures, *Langmuir*, *30*(18), 5142–5151.
Carminati, A., A. Kaestner, P. Lehmann, and H. Flühler (2008), Unsaturated water flow across soil aggregate contacts, *Adv. Water Resour.*, *31*(9), 1221–1232.
Carpenter, T. A., E. S. Davies, C. Hall, L. D. Hall, W. D. Hoff, and M. A. Wilson (1993), Capillary water migration in rock: Process and material properties examined by NMR imaging, *Mater. Struct.*, *26*(5), 286–292.
Chen, Q., M. K. Gingras, and B. J. Balcoma (2003), A magnetic resonance study of pore filling processes during spontaneous imbibition in Berea sandstone, *J. Chem. Phys. 119*(18), 9609–9616.
Cheng, C. L., E. Perfect, B. Donnelly, H. Z. Bilheux, A. S. Tremsin, L. D. McKay, V. H. DiStefano, J. C. Cai, and L. J. Santodonato (2015), Rapid imbibition of water in fractures within unsaturated sedimentary rock, *Adv. Water Resour.*, *77*, 82–89.
Czachor, A., E. El-Abd, and J. Milczarek (2002), Determination of capillary motion of water in bricks using neutron radiography, *Acta Phys. Polon.*, *102*(2), 245–252.
David, C., B. Menéndez, and J.-M. Mengus (2008), Influence of mechanical damage on fluid flow patterns investigated using CT scanning imaging and acoustic emissions techniques, *Geophys. Res. Lett.*, *35*, L16313, doi:10.1029/2008GL034879.
David, C., B. Menéndez, and J. M. Mengus (2011), X-ray imaging of water motion during capillary imbibition: Geometry and kinetics of water front in intact and damaged porous rocks, *J. Geophys. Res.*, *116*, B03204, doi:10.1029/2010JB007972.
Deinert, M. R., J. Y. Parlange, T. Steenhuis, J. Throop, K. Ünlü, and K. B. Cady (2004), Measurement of fluid contents and wetting front profiles by real-time neutron radiography, *J. Hydrol.*, *290*(3–4), 192–201.
Dewanckele, J., T. De Kock, G. Fronteau, H. Derluyn, P. Vontobel, M. Dierick, L. Van Hoorebeke, P. Jacobs, and V. Cnudde (2014), Neutron radiography and X-ray computed tomography for quantifying weathering and water uptake processes inside porous limestone used as building material, *Mater. Charact.*, *88*, 86–99.
Doster, F., J. M. Nordbotten, and M. A. Celia (2013), Impact of capillary hysteresis and trapping on vertically integrated models for CO_2 storage, *Adv. Water Resour.*, *62*(2), 465–474.
Doyen, P. M. (1988), Permeability, conductivity, and pore geometry of sandstone, *J. Geophys. Res.*, *93*(93), 7729–7740.
Dullien, F. A. L., M. S. El-Sayed, and V. K. Batra (1977), Rate of capillary rise in porous media with nonuniform pores, *J. Colloid Interface Sci.*, *60*(3), 497–506.
El Abd, A., A. Czachor, and J. Milczarek (2009), Neutron radiography determination of water diffusivity in fired clay brick, *Appl. Radiat. Isot.*, *67*(4), 556–559.
Faybishenko, B., P. A. Witherspoon, and J. Gale (2005), *Dynamics of Fluids and Transport in Fractured Rock*, pp. 1–11, AGU, Washington, D. C.
Feng, Y., B. Yu, M. Zou, and D. Zhang (2004), A generalized model for the effective thermal conductivity of porous media based on self-similarity, *J. Phys. D: Appl. Phys.*, *37*(21), 3030–3040.
Ferguson, H., and W. H. Gardner (1963), Diffusion theory applied to water flow data obtained using gamma ray Absorption1, *Soil Sci. Soc. Am. J.*, *27*(3), 243–246.
Gruener, S., Z. Sadjadi, H. E. Hermes, A. V. Kityk, K. Knorr, S. U. Egelhaaf, H. Rieger, and P. Huber (2012), Anomalous front broadening during spontaneous imbibition in a matrix with elongated pores, *Proc. Natl. Acad. Sci. U.S.A.*, *109*(26), 10245–10250.
Haber-Pohlmeier, S., S. Stapf, D. Van Dusschoten, and A. Pohlmeier (2010), Relaxation in a natural soil: Comparison of relaxometric imaging, T1–T2 correlation and fast-field cycling NMR, *Open Magn. Reson. J.*, *3*(1), 57–62.
Hall, C., and W. D. Hoff (2012), *Water Transport in Brick, Stone and Concrete*, 2nd ed., pp. 30–61, Spon Press, London.
Hall, S. A. (2013), Characterization of fluid flow in a shear band in porous rock using neutron radiography, *Geophys. Res. Lett.*, *40*, 2613–2618 doi:10.1002/grl.50528.
Hall, S. A., D. Hughes, and S. Rowe (2010), Local characterisation of fluid flow in sandstone with localised deformation features through fast neutron imaging, *EPJ Web of Conferences*, *6*, 22008.
Hammecker, C., and D. Jeannette (1994), Modelling the capillary imbibition kinetics in sedimentary rocks role of petrographical features, *Transp. Porous Media*, *17*(3), 19.
Hammecker, C., L. Barbiero, P. Boivin, J. L. Maeght, and E. H. B. Diaw (2004), A geometrical pore model for estimating the Microscopical pore geometry of soil with infiltration measurements, *Transp. Porous Media*, *54*(2), 193–219.
Han, S., M. Wu, H. Wang, L. Hao, G. Wei, L. He, Y. Wang, Y. Liu, and D. Chen (2013), Design of Cold Neutron Imaging Facility at China Advanced Research Reactor, *Physics Procedia*, *43*, 73–78.
Hassanein, R., H. O. Meyer, A. Carminati, M. Estermann, E. Lehmann, and P. Vontobel (2006), Investigation of water imbibition in porous stone by thermal neutron radiography, *J. Phys. D: Appl. Phys.*, *39*(19), 4284–4291.
Herring, A. L., E. J. Harper, L. Andersson, A. Sheppard, B. K. Bay, and D. Wildenschild (2013), Effect of fluid topology on residual nonwetting phase trapping: Implications for geologic CO_2 sequestration, *Adv. Water Resour.*, *62*(4), 47–58.
Hunt, J. R., and A. F. Tompson (2005), Tracing long-term vadose zone processes at the Nevada Test Site, USA, *Hydrol. Process.*, *19*(17), 3383–3394.
Jasti, J. K., J. T. Lindsay, and H. S. Fogler. (1987), Flow imaging in porous media using neutron radiography, in *SPE Annual Technical Conference and Exhibition*, edited, Society of Petroleum Engineers.

Jelinkova, V., M. Snehota, A. Pohlmeier, D. van Dusschoten, and M. Cislerova (2011), Effects of entrapped residual air bubbles on tracer transport in heterogeneous soil: Magnetic resonance imaging study, *Org. Geochem*. *42*, 991–998.
Joekar-Niasar, V., M. Prodanović, D. Wildenschild, and S. M. Hassanizadeh (2010), Network model investigation of interfacial area, capillary pressure and saturation relationships in granular porous media, *Water Resour. Res.*, *46*, W06526, doi:10.1029/2009WR008585.
Kang, M., E. Perfect, C. L. Cheng, H. Z. Bilheux, M. Gragg, D. M. Wright, J. M. Lamanna, J. Horita, and J. M. Warren (2013), Diffusivity and Sorptivity of Berea sandstone determined using neutron radiography, *Vadose Zone J.*, *12*(3), 1712–1717.
Kang, M., E. Perfect, C. L. Cheng, H. Z. Bilheux, J. Lee, J. Horita, and J. M. Warren (2014), Multiple pixel-scale soil water retention curves quantified by neutron radiography, *Adv. Water Resour.*, *65*, 1–8.
Kao, C. S., and J. R. Hunt (1996), Prediction of wetting front movement during one-dimensional infiltration into soils, *Water Resour. Res.*, *32*(1), 55–64.
Karoglou, M., A. Moropoulou, A. Giakoumaki, and M. K. Krokida (2005), Capillary rise kinetics of some building materials, *J. Colloid Interface Sci.*, *284*(1), 260–264.
Karpyn, Z. T., P. M. Halleck, and A. S. Grader (2009), An experimental study of spontaneous imbibition in fractured sandstone with contrasting sedimentary layers, *J. Pet. Sci. Eng.*, *67*(1–2), 48–56.
Katz, A. J., and A. H. Thompson (1985), Fractal sandstone pores: Implications for conductivity and pore formation, *Phys. Rev. Lett.*, *54*(12), 1325–1328.
Kim, F. H., D. Penumadu, and D. S. Hussey (2012), Water distribution variation in partially saturated granular materials using neutron imaging, *J. Geotech. Geoenviron.*, *138*(2), 147–154.
Kim, F. H., D. Penumadu, J. Gregor, N. Kardjilov, and I. Manke (2013), High-resolution neutron and X-ray imaging of granular materials, *J. Geotech. Geoenviron.*, *139*(5), 715–723.
Korvin, G. (2016), Permeability from microscopy: Review of a dream, *Arab. J. Sci. Eng.*, *41*(6), 2045–2065.
Krohn, C. E. (1988), Fractal measurements of sandstones, shales, and carbonates, *J. Geophys. Res.*, *93*(B4), 3297–3305.
Leech, C., D. Lockington, and P. Dux (2003), Unsaturated diffusivity functions for concrete derived from NMR images, *Mater. Struct.*, *36*(6), 413–418.
Leventis, A., D. A. Verganelakis, M. R. Halse, and J. B. Webber (2000), Capillary imbibition and pore characterisation in cement pastes, *Transp. Porous Media*, *39*(2), 143–157.
Lewandowski, R., L. Cao, and D. Turkoglu (2012), Noise evaluation of a digital neutron imaging device, *Nucl. Instrum. Methods Phys. Res., Sect. A*, *674*, 46–50.
Li, K., and R. N. Horne (2001), Characterization of spontaneous water imbibition into gas-saturated rocks, *SPE J.*, *6*(4), 375–384.
Li, K., and H. Zhao (2011), Fractal prediction model of spontaneous imbibition rate, *Transp. Porous Media*, *91*(2), 363–376.
Li, K., and R. N. Horne (2013), An analytical scaling method for spontaneous imbibition in gas/water/rock systems, *SPE J.*, *9*(03), 322–329.
Lucas, R. (1918), Rate of capillary ascension of liquids, *Kolloid Z.*, *23*(15), 15–22.
Nabawy, B. S., and C. David (2016), X-ray CT scanning imaging for the Nubia sandstone as a tool for characterizing its capillary properties, *Geosci. J.*, *20*(5), 691–704.
Nielsen, A. F. (1972), Gamma-ray-attenuation used for measuring the moisture content and homogeneity of porous concrete, *Build. Sci.*, *7*(4), 257–263.
Nizovtsev, M. I., S. V. Stankus, A. N. Sterlyagov, V. I. Terekhov, and R. A. Khairulin (2008), Determination of moisture diffusivity in porous materials using gamma-method, *Int. J. Heat Mass Transfer*, *51*(17–18), 4161–4167.
Otsu, N. (1979), A threshold selection method from gray-level histograms, *IEEE Trans. Syst. Man Cybern.*, *9*(1), 62–66.
Pease, B. J., G. A. Scheffler, and H. Janssen (2012), Monitoring moisture movements in building materials using X-ray attenuation: Influence of beam-hardening of polychromatic X-ray photon beams, *Constr. Build. Mater.*, *36*(3), 419–429.
Perfect, E., C. L. Cheng, M. Kang, H. Z. Bilheux, J. M. Lamanna, M. J. Gragg, and D. M. Wright (2014), Neutron imaging of hydrogen-rich fluids in geomaterials and engineered porous media: A review, *Earth Sci. Rev.*, *129*, 120–135.
Philip, R. J. (1957), The theory of infiltration: 4. Sorptivity and algebraic infiltration equations, *Soil Sci.*, *84*(3), 257–264.
Pickard, W. F. (1981), The ascent of sap in plants, *Prog. Biophys. Mol. Biol.*, *37*(37), 181–229.
Pohlmeier, A., A. Orospeusquens, M. Javaux, M. I. Menzel, J. Vanderborght, J. Kaffanke, S. Romanzetti, J. Lindenmair, H. Vereecken, and N. J. Shah (2008a), Changes in soil water content resulting from root uptake monitored by magnetic resonance imaging, *Vadose Zone J.*, *7*(3), 1010–1017.
Pons, A., C. David, J. Fortin, S. Stanchits, B. Menéndez, and J. M. Mengus (2011), X-ray imaging of water motion during capillary imbibitions: A study on how compaction bands impact fluid flow in Bentheim sandstone, *J. Geophys. Res.*, *116*, B03205, doi:10.1029/2010JB007973.
Rasband, W. S. (1997-2016), *ImageJ, U.S. National Institutes of Health*, Bethesda, Md. [Available at https://imagej.nih.gov/ij/.]
Richards, L. A. (1931), Capillary conduction of liquids through porous mediums, *J. Appl. Phys.*, *1*(5), 318–333.
Roels, S., and J. Carmeliet (2006), Analysis of moisture flow in porous materials using microfocus X-ray radiography, *Int. J. Heat Mass Transfer*, *49*(25–26), 4762–4772.
Roels, S., J. Carmeliet, H. Hens, O. C. G. Adan, H. J. P. Brocken, R. Cerny, Z. Pavlik, A. T. Ellis, C. Hall, and K. Kumaran (2004), A comparison of different techniques to quantify moisture content profiles in porous building materials, *J. Therm. Envel. Build. Sci.*, *27*(4), 261–276.
Sahimi, M. (2011), *Flow and Transport in Porous Media and Fractured Rock: From Classical Methods to Modern Approaches*, 2nd ed., pp. 1–7,143, Wiley-VCH, Weinheim, Germany.
Schillaci, T., M. Brai, A. Cimino, and A. L. Casto (2008), Study of capillary absorption kinetics by X-ray CT imaging techniques: A survey on sedimentary rocks of Sicily, *Conserv. Sci. Cult. Heri. Historical Tech. J.*, *8*(1), 91–110.
Schneider, C. A., W. S. Rasband, and K. W. Eliceiri (2012), NIH image to ImageJ: 25 years of image analysis, *Nat. Methods*, *9*(7), 671–675.
Sekkat, Z., H. Ishitobi, M. Tanabe, T. Hiramatsu, and S. Kawata (2011), On the application of focused ion beam nanotomography in characterizing the 3D pore space geometry of Opalinus clay, *Phys. Chem. Earth*, *36*(17), 1539–1544.
Singh, H. (2016), A critical review of water uptake by shales, *J. Nat. Gas Sci. Eng.*, *34*, 751–766.
Tidwell, V. C., L. C. Meigs, T. Christian-Frear, and C. M. Boney (2000), Effects of spatially heterogeneous porosity on matrix diffusion as investigated by X-ray absorption imaging, *J. Contam. Hydrol.*, *42*(2–4), 285–302.
Tompson, A. F. B., G. B. Hudson, D. K. Smith, and J. R. Hunt (2006), Analysis of radionuclide migration through a 200-m vadose zone following a 16-year infiltration event, *Adv. Water Resour.*, *29*(2), 281–292.
Tullis, B. P., J. T. Lindsay, and S. J. Wright (1994), The imaging of wetting front instabilities in porous media using neutron radioscopy, *Nondestruct. Test. Eval.*, *11*(2–3), 97–106.
Vasin, M., P. Lehmann, A. Kaestner, R. Hassanein, W. Nowak, R. Helmig, and I. Neuweiler (2008), Drainage in heterogeneous sand columns with different geometric structures, *Adv. Water Resour.*, *31*(9), 1205–1220.

Wadell, H. (1935), Volume, shape, and roundness of quartz particles, *J. Geol.*, *43*, (3), 250–280.
Washburn, E. W. (1921), The dynamics of capillary flow, *Phys. Rev.*, *17*(3), 273–283.
Wong, P. Z., J. Koplik, and J. P. Tomanic (1984), Conductivity and permeability of rocks, *Phys. Rev. B: Condens. Matter*, *30*(11), 6606–6614.
Xie, J., Z. Ke-ni, W. Yong-sheng, Q. Li-qing, and G. Chao-Bin (2016), Performance assessment of CO_2 geological storage in deep saline aquifers in Ordos Basin, China, *Rock and Soil Mechanics*(1), 166–174+184.
Yu, B., P. Xu, M. Zhou, J. Cai, and Q. Zheng (2014), *Fractal Porous Media Transport*, pp. 247–268, Science Press, Beijing.
Zhang, L., Q. J. Kang, J. Yao, Y. Gao, Z. X. Sun, H. H. Liu, and A. J. Valocchi (2015), Pore scale simulation of liquid and gas two-phase flow based on digital core technology, *SCIENCE CHINA Technol. Sci.*, *58*(8), 1375–1384.
Zhang, P., F. H. Wittmann, T. Zhao, and E. H. Lehmann (2010), Neutron imaging of water penetration into cracked steel reinforced concrete, *Phys. B*, *405*(7), 1866–1871.